Inorganic Chemistry

Article

pubs.acs.org/IC

The First Vanadate−Carbonate, $K_2Mn_3(VO_4)_2(CO_3)$: Crystal Structure and Physical Properties

Olga V. Yakubovich, Ekaterina V. Yakovleva, Alexey N. Golovanov, Anatoly S. Volkov, Olga S. Volkova, Elena A. Zvereva, Olga V. Dimitrova, and Alexander N. Vasiliev*

M. V. Lomonosov Moscow State University, Moscow 119991, Russia

Supporting Information

ABSTRACT: Mixed potassium−manganese vanadate−carbonate, $K_2Mn_3(VO_4)_2(CO_3)$, represents a novel structure type; it has been synthesized hydrothermally from the system $MnCl_2-K_2CO_3-V_2O_5-H_2O$. Its hexagonal crystal structure was determined by single-crystal X-ray diffraction with $a = 5.201(1)$ Å, $c = 22.406(3)$ Å, space group $P6_3/m$, $Z = 2$, $\rho_c = 3.371$ g/cm^3, and $R = 0.022$. The layered structure of the compound can be described as a combination of honeycomb-type modules of $[MnO_6]$ octahedra and $[VO_4]$ tetrahedra, alternating in the [001] direction with layers of $[MnCO_3]$ built by $[MnO_5]$ trigonal bipyramids and $[CO_3]$ planar triangles, sharing oxygen vertices. The K^+ ions are placed along channels of the framework, elongated in the [100], [010], and [110] directions. The title compound exhibits rich physical properties reflected in a phase transition of presumably Jahn−Teller origin at $T_3 = 80-100$ K as well as two successive magnetic phase transitions at $T_2 = 3$ K and $T_1 = 2$ K into a weakly ferromagnetic ground state, as evidenced in magnetization, specific heat, and X-band electron spin resonance measurements. A negative Weiss temperature $\Theta = -114$ K and strongly reduced effective magnetic moment $\mu_{\text{eff}}^2 \sim 70\ \mu_B^2$ per formula unit suggest that antiferromagnetic exchange interactions dominate in the system. Divalent manganese is present in a high-spin state, $S = {}^5/_2$, in the octahedral environment and a low-spin state, $S = {}^1/_2$, in the trigonal-bipyramidal coordination.

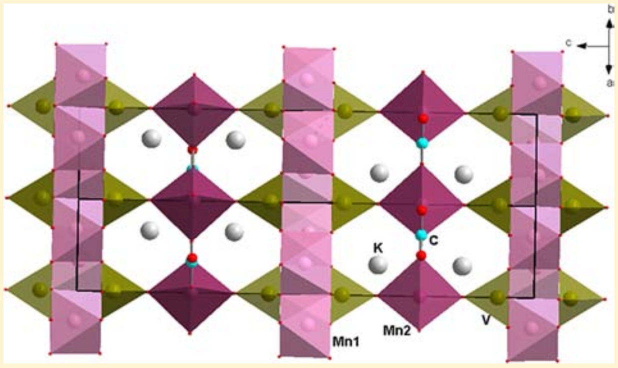

INTRODUCTION

Several recently synthesized mixed-metal oxides contain structural units similar to those found in one of the mineral forms of aluminum hydroxide $Al(OH)_3$: gibbsite.[1] The basic structure of gibbsite forms stacked sheets of linked octahedra, which are composed of Al^{3+} ions bonded to six octahedrally coordinated hydroxides. Each of the hydroxides is bonded to only two metal ions because one-third of the octahedra do not contain Al^{3+} ions in their centers. From the "magnetic" point of view, this structure is analogous to a honeycomb network when the positions in the octahedral surroundings are occupied by ions of the transition metal. These types of structures were recently found in the focus of fundamental research in quantum physics.[2,3] This interest is due to their reduced magnetic dimensionality and inherent frustration, preventing the formation of long-range magnetic order even at lowest temperatures.[4] Among recent advances in the field of low-dimensional and frustrated magnetism in honeycomb lattice systems are observations of a spin glass state in $Bi_3Mn_4O_{12}(NO_3)$ and the formation of an antiferromagnetic ground state in monoclinic $Li_3Ni_2SbO_6$, despite the predominance of ferromagnetic interactions at elevated temperatures.[5,6] In search of new systems belonging to this class of compounds, we synthesized potassium−manganese vanadate−carbonate, $K_2Mn_3(VO_4)_2(CO_3)$, and studied its physical properties over a wide range of temperatures and magnetic fields.

CRYSTAL GROWTH AND CRYSTAL STRUCTURE DETERMINATION

Translucent red-orange crystals of the title compound with a hexagonal-prismatic shape were prepared by employing hydrothermal synthesis. A mixture of $MnCl_2$, K_2CO_3, V_2O_5, and H_2O in a weight ratio of 1:1:1:30 was placed in a 4 mL poly(tetrafluoroethylene)-lined stainless steel autoclave. A small amount of boric anhydride (0.05 g) was added to the starting mixture as a mineralizer. The system was kept at $T = 280$ °C and $P = 70$ bar for 18 days. The presence of Mn, V, K, and O in the samples was confirmed by semiquantitative X-ray spectroscopic microanalysis (Jeol JSM-6480LV; energy-dispersive X-ray spectrometer INCA-Wave 500).

Crystallographic data and X-ray experimental parameters are given in Table 1. The reflection intensities (full sphere of reciprocal space) were corrected for Lorentz and polarization effects. An empirical absorption correction was applied by modeling the shape of the single crystal. The atomic scattering curves and anomalous dispersion corrections were taken from

Received: October 25, 2012
Published: January 18, 2013

Table 1. Crystal Data and Details of the X-ray Data Collection and Refinement

Crystal Data	
chemical formula, M/g mol^{-1}	$K_2Mn_3[VO_4]_2(CO_3)$, 532.91
cryst syst, space group	hexagonal, $P6_3/m$ (No. 176)
a, b, c/Å; α, β, γ/deg	5.201(1), 5.201(1), 22.406(3); 90, 90, 120
V/Å^3, Z	524.9(2), 2
D_c/g cm^{-3}	3.371
cryst size/mm^3	0.05 × 0.11 × 0.14
cryst color	red-orange
abs coeff μ/mm^{-1}	6.07
Data Collection	
diffractometer	Xcalibur-S, CCD
radiation	Mo Kα (λ = 0.71073 Å), graphite monochromator
temperature/K	293
scanning mode	$\omega/2\theta$
$2\theta_{max}$/deg	59.94
no. of measd reflns	9623
R_{int}, $R(\sigma)$	0.0353, 0.0119
h, k, l range	$-7 \le h \le 7$, $-7 \le k \le 7$, $-31 \le l \le 31$
Refinement	
program used to refine the structure	*SHELXL*
refinement on	F^2
reflns unique, obsd [$I > 2\sigma(I)$]	530, 535
no. of param used in the refinement	33
abs corrn	numerical
T_{max}, T_{min}	0.737, 0.535
R value [$F_{obs} > 4\sigma(F_{obs})$]	R1 = 0.0222, wR2 = 0.0562
R value (all data)	R1 = 0.0226, wR2 = 0.0563
GOF	1.568
largest diff peak, hole/e Å^{-3}	0.428, −0.891

the *International Crystallographic Tables*.[7] All of the calculations were performed using the *Wingx32* software package.[8] Crystal structures were solved using the *SUPERFLIP* program[9] and refined in an anisotropic approximation of the ions' thermal vibrations (*SHELXL*[10]). The positions of the C^{4+} ions that were not identified in the crystal composition by microprobe analysis but participated in the system of crystallization have been found using the difference Fourier synthesis. We also found that the crystal under investigation presented a merohedral twin with a 2-fold pseudoaxis aligned in the [110] direction. Refinement of the crystal structure yielded a twinning parameter of 0.372(4). Table 2 presents the final results for the atom positions and equivalent displacement parameters. Characteristic distances are given in Table 3. The $K_2Mn_3(VO_4)_2(CO_3)$ compound shows a novel structure type. The results of the bond-valence calculation, presented in Table 4, are consistent with the assumed oxidation states of Mn^{2+} and V^{5+}.

Table 2. Atomic Coordinates and Equivalent Isotropic Displacement Parameters (Å^2)

atom	x/a	y/b	z/c	U_{eq}
V	0.0	0.0	0.07987(2)	0.00583(14)
Mn1	0.66667	0.33333	0.00457(2)	0.00810(14)
Mn2	0.0	0.0	0.25	0.01058(16)
K	0.33333	0.66667	0.15776(3)	0.01513(17)
C	0.66667	0.33333	0.25	0.0086(7)
O1	0.0	0.0	0.15520(1)	0.0152(5)
O2	0.4434(4)	0.0681(4)	0.25	0.0138(4)
O3	0.3098(3)	−0.0106(3)	0.05494(5)	0.0092(2)

■ INTERATOMIC DISTANCES AND CRYSTAL STRUCTURE DESCRIPTION

Figure 1 shows the basic structural units of $K_2Mn_3(VO_4)_2(CO_3)$. The Mn^{2+} ions in the structure form two types of polyhedra: octahedra and five-vertex polyhedra. The interatomic Mn−O distances in the Mn1 octahedra (site symmetry C_3) vary from 2.144(1) to 2.195(1) Å. The morphology of Mn2 five-vertex polyhedra (site symmetry C_{3h}) can be defined as trigonal-bipyramidal; here the range of distances is smaller: 2.124(2)−2.151(2) Å. In the VO_4 tetrahedra, three bond lengths are equal to each other, V−O = 1.732(1) Å, while the fourth bond length is much shorter, 1.688(2) Å. The C−O distance in the regular CO_3 triangles is 1.284(2) Å, and the O−C−O angle is 120°. In the nine-vertex K polyhedra, the K−O distances are divided into three groups with bond lengths 2.787(1), 2.889(1), and 3.003(1) Å (Table 3).

The crystal structure framework of the new phase is formed by two types of layers alternating along the c axis of the hexagonal unit cell, as shown in Figure 2. The first layer parallel to the ab plane consists of honeycomb layers of Mn1 octahedra sharing cis and trans edges (Figure 3a). The second one consists of Mn2 trigonal bipyramids linked by $[CO_3]$ triangles forming cellular layers (Figure 3b).

The $[VO_4]$ tetrahedra share oxygen vertices with manganese polyhedra, thus linking the layers along the c axis. Intercrossing channels intersect the structure in the [100], [010], and [110] directions; the K^+ ions are located in these channels. The $K_2Mn_3(VO_4)_2(CO_3)$ crystal structure may be formally considered as a derivative of the $BaNi_2(VO_4)_2$ structure type. In the trigonal $BaNi_2(VO_4)_2$,[11] similar structural fragments built of $[NiO_6]$ and $[VO_4]$ polyhedra are shifted to each other along the [110] direction by R lattice translation. Along the c axis, they alternate with layers of Ba^{2+} cations (Figure 4). Thus, upon extraction of the $[MnCO_3]_\infty$ layers from the structure of $K_2Mn_3(VO_4)_2(CO_3)$ with simultaneous exchange of Mn^{2+} ions for Ni^{2+} ions in octahedra and of one Ba^{2+} ion for two K^+ ions in the interlayer space, the $BaNi_2(VO_4)_2$ structure is obtained.

Our compound presents the first vanadate−carbonate published so far at least as a novel crystal structure. Its closest relatives, phosphate−carbonates, are also very rare, to our knowledge. At the moment, we can mention only two types of synthetic phases belonging to this crystal chemical family. These are analogues of the mineral carbonate−apatite obtained during high-pressure experiments or by solid-state reaction.[12,13] Recently, powder samples of seven phosphate−carbonates with the general formula $Na_3M(PO_4)(CO_3)$ (M = Mg, Mn, Fe, Co, Ni, Cu, Sr) have been hydrothermally synthesized. Rietveld refinements were performed for high-resolution synchrotron X-ray diffraction patterns of the Fe, Mn, Co, and Ni varieties, using the mineral sidorenkite as a structure model.[14] There are literature data of about 10 crystal structures of minerals phosphate−carbonates, besides carbonate−apatite. Only one among them, the mineral sidorenkite, $Na_3Mn(PO_4)(CO_3)$,[15] is compositionally similar to $K_2Mn_3(VO_4)_2(CO_3)$, but no one phosphate−carbonate may be cited as having structural resemblance with the title compound.

Table 3. Interatomic Distances (Å)

V tetrahedron		Mn1 octahedron		Mn2 polyhedron	
V–O1	1.688(2)	Mn1–O3	2.144(1) × 3	Mn2–O1	2.124(2) × 2
V–O3	1.732(1) × 3	Mn1–O3′	2.194(1) × 3	Mn2–O2	2.151(2) × 3
⟨V–O⟩	1.721	⟨Mn1–O⟩	2.169	⟨Mn2–O⟩	2.140

K polyhedron		C triangle	
K–O2	$2.786_5(1)$ × 3	C–O2	1.284(2) × 3
K–O3	2.888(1) × 3	⟨C–O⟩	1.284
K–O1	3.003_5 × 3		
⟨K–O⟩	2.893		

Table 4. $K_2Mn_3[VO_4]_2(CO_3)$ Bond-Valence Data[21a]

atom	V	Mn1	Mn2	K	C	Σ
O1	1364		$0.405_{\downarrow 2}$	$0.094_{\downarrow 3}$		1863
O2			$0.377_{\downarrow 3}$	$0.17_{\downarrow 3}$	$1332_{\downarrow 3}$	1879
O3	$1212_{\downarrow 3}$	$0.384_{\downarrow 3}$; $0.335_{\downarrow 3}$		$0.129_{\downarrow 3}$		2060
Σ	5000	2157	1.941	1.179	3996	

[a] Values marked by $_{\downarrow 2}$ and $_{\downarrow 3}$ contribute two and three times, respectively, to the sum along the column by symmetry.

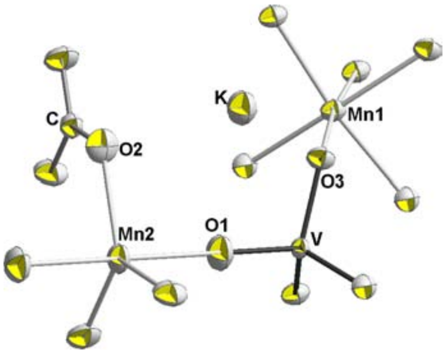

Figure 1. Main structural elements in $K_2Mn_3(VO_4)_2(CO_3)$. Displacement ellipsoids are drawn at the 90% probability level.

■ MAGNETIC, THERMAL, AND RESONANCE MEASUREMENTS

The magnetic and thermal properties of $K_2Mn_3(VO_4)_2(CO_3)$ were measured using a Physical Property Measurement System (Quantum Design PPMS) in the temperature range 2–300 K under a magnetic field of up to 9 T. Powder samples were obtained by crushing tiny single crystals of the title compound in an agate mortar. Electron spin resonance (ESR) studies were carried out using an X-band ESR spectrometer CMS 8400 (ADANI) ($f \approx 9.4$ GHz; $B \leq 0.7$ T) equipped with a low-temperature mount, operating in the range 6–300 K. The effective g factors have been calculated with respect to an external reference for the resonance field. We used *a*,*g*-bis(diphenyline)-*b*-phenylallyl (BDPA), $g_{ref} = 2.0036$, as a reference material.

The temperature dependence of the magnetic susceptibility $\chi = M/B$ in $K_2Mn_3(VO_4)_2(CO_3)$ at $B = 1$ T is shown in Figure 5. At elevated temperatures, the magnetic susceptibility follows the Curie–Weiss law with the addition of a temperature-independent term χ_0, i.e.

$$\chi = \chi_0 + C/(T - \Theta) \tag{1}$$

The best fit of the $\chi(T)$ curve in the range 200–300 K gives $\chi_0 = 3 \times 10^{-3}$ emu mol^{-1}, a Curie constant $C = 8.5$ emu mol^{-1} K^{-1}, the square of effective magnetic moment $\mu_{eff}^2 = 68\ \mu_B^2$ per formula unit, and Weiss temperature $\Theta = -114$ K. The negative sign of the Weiss temperature signals the dominance of antiferromagnetic interactions at high temperatures. At lowering temperature, however, the experimental curve strongly deviates from the Curie–Weiss fit, shown by the solid line in Figure 5. This deviation suggests strengthening of ferromagnetic interactions in the system. Moreover, at about 3 K, a sharp increase in the χ value indicates a transition into a weakly ferromagnetic state.

Inspection of the reciprocal magnetic susceptibility, shown in the right inset of Figure 5, reveals a drastic change of the slope

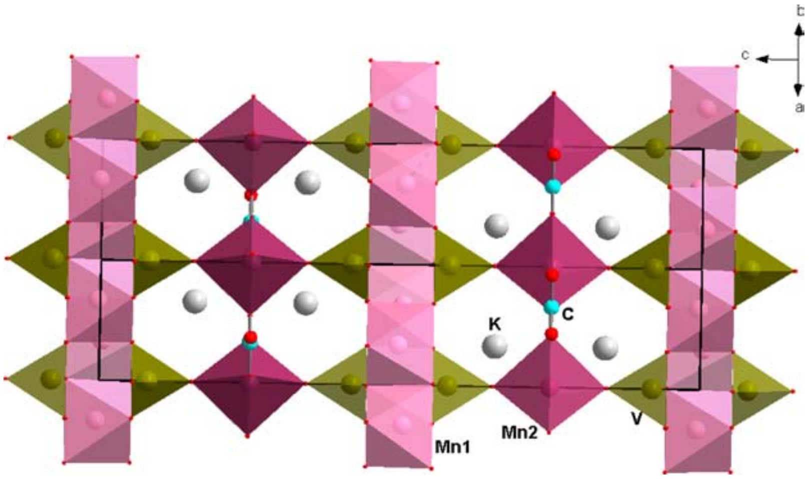

Figure 2. $K_2Mn_3(VO_4)_2(CO_3)$ crystal structure in the [110] projection.

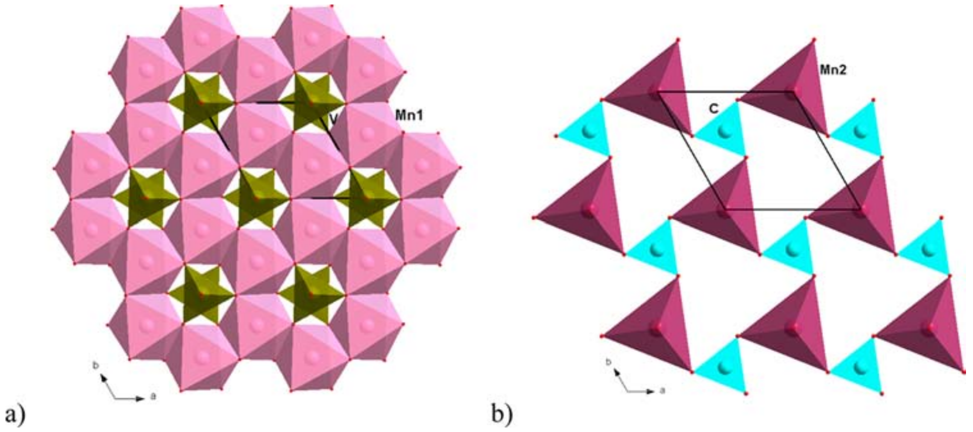

Figure 3. $K_2Mn_3(VO_4)_2(CO_3)$ crystal structure: (a) gibbsite-like layer of $[MnO_6]$ octahedra sharing edges and adjacent $[VO_4]$ tetrahedra; (b) layer formed by $[MnO_5]$ bipyramids and $[CO_3]$ triangle groups.

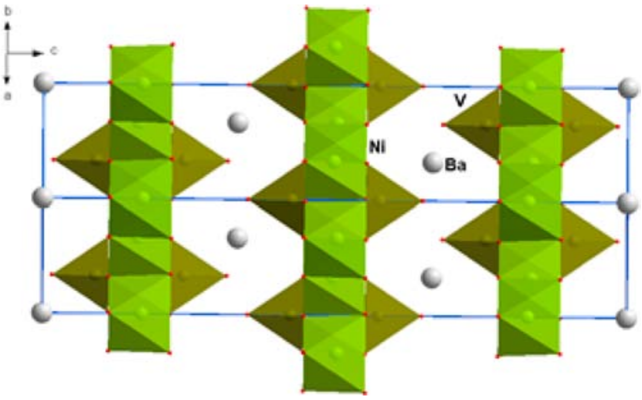

Figure 4. $BaNi_2(VO_4)_2$ crystal structure: blocks formed by layers of $[NiO_6]$ octahedra and $[VO_4]$ tetrahedra alternating with layers of Ba^{2+} ions along the *c* axis.

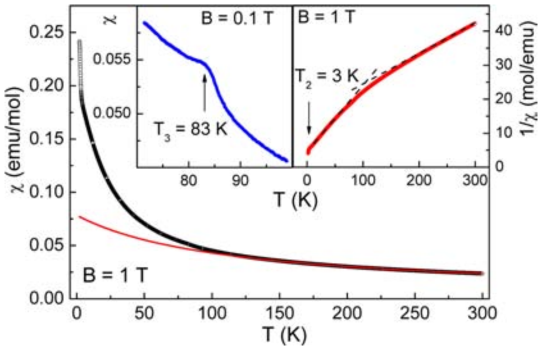

Figure 5. Temperature dependence of the magnetic susceptibility $\chi = M/B$ in $K_2Mn_3(VO_4)_2(CO_3)$ measured at $B = 1$ T. The right inset shows the inverse magnetic susceptibility $\chi^{-1}(T)$ over a wide temperature range. The slopes of this curve at low ($T < 100$ K) and high ($T > 100$ K) temperature are shown by dashed lines. The temperature dependence of the magnetic susceptibility χ measured at B = 0.1 T is shown in the left inset.

in the vicinity of 100 K. The left inset of Figure 5 shows part of the χ versus T curve taken at $B = 0.1$ T. A steplike anomaly in the magnetic susceptibility measured upon heating from low temperatures can be identified at $T_3 = 83$ K. The magnetization curve of $K_2Mn_3(VO_4)_2(CO_3)$ measured at $T = 2$ K as a function of the field up to 9 T demonstrates a plateaulike feature at intermediate magnetic fields and a sharp upturn in the magnetization at about $B_C = 7$ T. This behavior, shown in Figure 6, is not typical for a "simple" antiferromagnet and demands analysis of the relative strengths of exchange interactions between $Mn1^{2+}$ and $Mn2^{2+}$ ions and their spin states.

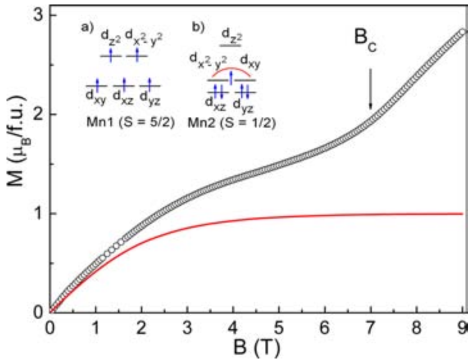

Figure 6. Field dependence of magnetization in $K_2Mn_3(VO_4)_2(CO_3)$ taken at $T = 2$ K. The solid line represents the Brillouin function for paramagnetic $S = {}^1/_2$ ions. The insets represent the crystal-field splitting of d shells in $Mn1^{2+}$ and $Mn2^{2+}$ ions (see the text).

Measurement of specific heat C of $K_2Mn_3(VO_4)_2(CO_3)$ in the range of 2−150 K gives additional information of its physical properties. It was found that the ordering of the magnetic subsystem takes place in two steps via phase transitions at $T_1 = 2$ K and $T_2 = 3$ K. Similar two-step transitions are found in low-dimensional magnetic systems and are frequently identified in neutron scattering measurements as the formation of magnetic incommensurate phases at T_2 and commensurate phases at T_1.[16,17] As shown in Figure 7, these anomalies are seen on the background of a wide Schottky-type anomaly whose origin also needs consideration of the magnetic interactions in the title compound. We should note, however, that the anomaly at T_3 was not detected in relaxation-type specific-heat measurements.

Evolution of the ESR spectra in a powder sample of $K_2Mn_3(VO_4)_2(CO_3)$ taken during cooling from room temperature is shown on Figure 8. The ESR spectra are well described by single Lorentzian lines attributed to Mn^{2+} ions. At room temperature, the effective g factor is $g = 1.978$, being less than the free electron value $g = 2.0023$ typical for divalent manganese in the $S = 5/2$ high-spin state.

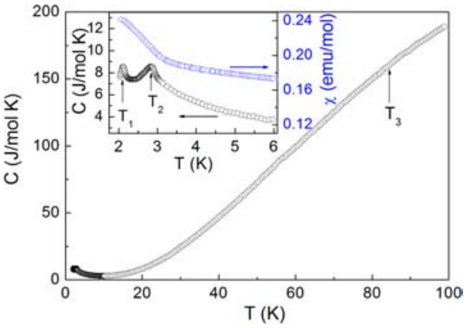

Figure 7. Temperature dependence of the specific heat in $K_2Mn_3(VO_4)_2(CO_3)$. The inset magnifies the low-temperature parts of the specific heat and magnetization curves.

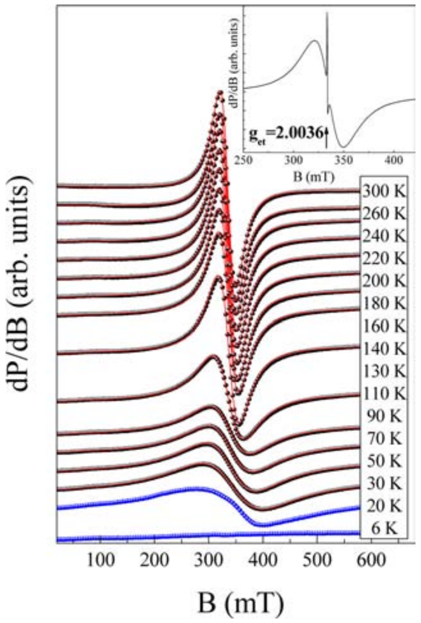

Figure 8. Temperature evolution of the first derivative of the absorption line in the powder sample of $K_2Mn_3(VO_4)_2(CO_3)$: black points, experimental data; solid lines, fitting in accordance with the Lorentzian profile. Inset: ESR spectrum of $K_2Mn_3(VO_4)_2(CO_3)$ recorded with the reference sample BDPA (g = 2.0036) at room temperature.

Upon cooling, the intensity of the ESR signal increases. Then, a gradual deviation of the ESR signal shape from the Lorentzian form as well as broadening occurs, indicating tentatively the suppression of exchange narrowing due to slowing of the spin−spin correlations upon approach to the short-range ordering regime. At the lowest temperatures achieved, the X-band ESR signal eventually vanishes, indicating the opening of an energy gap for resonance excitations approaching the formation of long-range magnetic order.

Temperature dependencies of the main ESR parameters derived from the Lorentzian fitting are collected in Figure 9. Evidently, every feature of the spectra, i.e., effective g factor, the line width ΔB, and the integral ESR intensity χ_{ESR} (which is proportional to the number of magnetic spins and was estimated by double integration of the first derivative of ESR spectra), detects anomalous behavior, revealing the distinct changes in their temperature-dependent character at around $T \sim 100$ K.

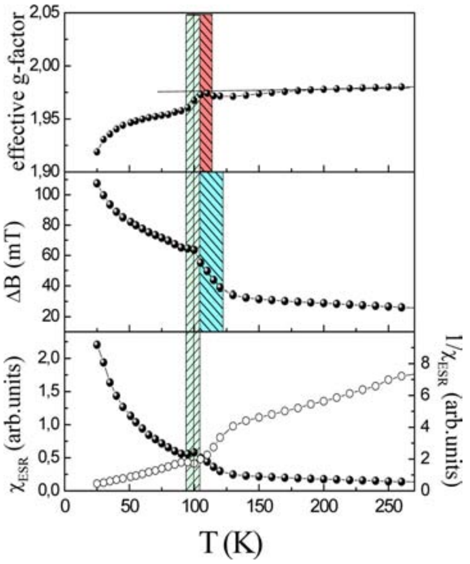

Figure 9. Temperature dependencies of the effective g factor (upper panel), ESR line width ΔB (middle panel), and direct and inverse ESR integral intensity χ_{ESR} (lower panel).

■ DISCUSSION

Let us discuss now specific features of the magnetic subsystem in $K_2Mn_3(VO_4)_2(CO_3)$. The honeycomb-type layers of $[MnO_6]$ octahedra linked through cis and trans edges form a dominating magnetic subsystem in the structure with presumably[18] strong antiferromagnetic interactions between $Mn1^{2+}$ ions. These ions in octahedral coordination are most probably in the high-spin state, $S = {}^5/_2$, as shown in the inset of Figure 6. The $Mn2^{2+}$ ions in a trigonal-bipyramidal environment are tentatively in the low-spin state, $S = {}^1/_2$, as is also shown in the inset of the same Figure 6. The combination of the magnetic moments of two $Mn1^{2+}$ and one $Mn2^{2+}$ ions at g = 1.978 gives the square of the effective magnetic moment $\mu_{eff}^2 = 71\ \mu_B^2$ per formula unit, which is in correspondence with the experimentally found value $\mu_{eff}^2 = 68\ \mu_B^2$. The observations of a low-spin state, $S = {}^1/_2$, in divalent Mn^{2+} ions are rather rare.[19,20] In the trigonal-bipyramidal environment, it can only be realized in the case when the d_{z^2} orbital is shifted upward significantly compared to the other magnetoactive orbitals.

The $Mn2^{2+}$ ions interact with $Mn1^{2+}$ ions through Mn1−O−V−O−Mn2 pathways and with each other via Mn2−O−C−O−Mn2 pathways; both these interactions are presumably significantly weaker than short Mn1−O−Mn1 ones. This makes the magnetic behavior of the $Mn2^{2+}$ ions dependent on the magnetization of the dominant Mn1 subsystem. Frustration of antiferromagnetic interactions in regular honeycomb-type layers of $Mn1^{2+}$ ions precludes the formation of long-range magnetic order in the system. Nevertheless, the system reaches magnetic ordering at low temperatures, exhibiting a rather large value of Neel (Curie) and Weiss temperatures $T_2/\Theta \sim 40$.

The anomaly seen in the magnetic susceptibility at T_S = 83 K being tentatively of Jahn−Teller origin can be responsible for the formation of long-range magnetic order at low temperatures. The distribution of five d electrons on degenerate orbitals of divalent manganese in a trigonal bipyramid is unstable with respect to Jahn−Teller distortion. Lifting of the degeneracy between d_{xy} and $d_{x^2-y^2}$ orbitals in $Mn2^{2+}$ ions should lead to a distortion of the crystal lattice in $K_2Mn_3(VO_4)_2(CO_3)$, therefore relieving frustration of the honeycomb-type layers of

$Mn1^{2+}$ ions. Evidently, this distortion should be rather small because no indication of this transition is seen in specific heat measurements. The ESR data corroborate this scenario. The fact that the anomalous behavior of ESR parameters is seen at higher temperatures (ca. 100 K) than the anomaly in the magnetic susceptibility χ (ca. 80K) probably indicates the difference in static and dynamic responses of the system to the phase transition.

The low values of the magnetic ordering temperatures T_1 and T_2 are related to the fact that the formation of long-range magnetic structure depends not only on the value of frustrated exchange interactions within the Mn1 layers but on the value of presumably weak exchange interactions between $Mn1^{2+}$ and $Mn2^{2+}$ ions as well. In a sense, the Mn2 subsystem can be considered "paramagnetic" magnetized by the dominant Mn1 subsystem. In this case, the magnetic level of $Mn2^{2+}$ ions is split by an internal magnetic field provided by $Mn1^{2+}$ ions through the Zeeman effect, therefore resulting in a broad Schottky-type anomaly in the specific heat. Accordingly, the steplike feature in magnetization of $K_2Mn_3(VO_4)_2(CO_3)$ at low temperatures can be attributed to the saturation of $S = {}^1/_2$ magnetic moments similar to the Brillouin function shown by a solid line in Figure 6.

CONCLUSIONS

We state that newly synthesized potassium−manganese vanadate−carbonate, $K_2Mn_3(VO_4)_2(CO_3)$, besides its unique structure type, demonstrates interesting physical properties related to the special arrangement of magnetically active manganese cations. The lift of frustration in the magnetic subsystem of this compound due to the presumed distortion of the crystal lattice at elevated temperature T_3 allows a two-step formation of long-range magnetic order at low temperatures. Further studies of this compound should provide additional information of the Mn^{2+} spin states in $K_2Mn_3(VO_4)_2(CO_3)$, reveal degree of structural distortion at the presumably Jahn−Teller type transition at T_3, and clarify features of presumably complicated magnetic structure at both lowest ($T < T_1$) and intermediate ($T_1 < T < T_2$) temperature ranges.

ASSOCIATED CONTENT

Supporting Information

Crystallographic data in CIF format. This material is available free of charge via the Internet at http://pubs.acs.org. CSD 425514 concerning the crystal structure determination has been sent to Fachinformationszentrum Karlsruhe, Hermann-von-Helmholtz-Platz 1, 76344 Eggenstein-Leopoldshafen, Germany, www.fiz-karlsruhe.de, and can be obtained by contacting the FIZ.

AUTHOR INFORMATION

Corresponding Author

*E-mail: vasil@mig.phys.msu.ru. Tel./fax: 007-4959329217.

Author Contributions

The manuscript was written through contributions of all authors. All authors have given approval to the final version of the manuscript. All authors contributed equally.

Notes

The authors declare no competing financial interest.

ACKNOWLEDGMENTS

We thank S. M. Kazakov and N. N. Karataeva for performing powder XRD and cation stoichiometry analysis of the samples studied and S. Rowley for critical reading of the manuscript. Support of the Russian Foundation for Basic Research through Grants 12-02-90823-mol-rf-nr, 10-02-00021, 10-05-01068, and 11-02-00083 is acknowledged.

REFERENCES

(1) Dewey, C. *Am. J. Sci. Arts* **1820**, *2*, 249−250.
(2) Kitaev, A. *Ann. Phys. (N.Y.)* **2006**, *321*, 2−111.
(3) Branford, W. R.; Ladak, S.; Read, D. E.; Zeissler, K.; Cohen, L. F. *Science* **2012**, *335*, 1597−1600.
(4) Chaloupka, J.; Jackeli, G.; Khaliullin, G. *Phys. Rev. Lett.* **2010**, *105*, 027204.
(5) Onishi, N.; Oka, K.; Azuma, M.; Shimakawa, Y.; Matome, Y.; Toniguchi, T.; Hiraishi, M.; Miyazaki, M.; Masuda, T.; Kodo, A.; Kojima, K. M.; Kadono, R. *Phys. Rev.* **2012**, *B 85*, 184412.
(6) Zvereva, E. A.; Evstigneeva, M. A.; Nalbandyan, V. B.; Savelieva, O. A.; Ibragimov, S. A.; Volkova, O. S.; Medvedeva, L. I.; Vasiliev, A. N.; Klingeler, R.; Buechner, B. *Dalton Trans.* **2012**, *41*, 572−580.
(7) *International Tables for Crystallography*, 3rd ed.; Prince, E., Ed.; Kluwer: Dordrecht, The Netherlands, 2004; Tables 4.2.6.8 and 6.1.14.
(8) Farrugia, L. J. *J. Appl. Crystallogr.* **1999**, *32*, 837−838.
(9) Palatinus, L.; Chapuis, G. *J. Appl. Crystallogr.* **2007**, *40*, 786−790.
(10) Sheldrick, G. M. *Acta Crystallogr.* **2008**, *A64*, 112−122.
(11) Wichmann, R.; Muller-Buschbaum H., H. *Rev. Chim. Miner.* **1984**, *21*, 824−829.
(12) Fleet, M. E.; Liu, Xi *J. Solid State Chem.* **2008**, *181*, 2494−2500.
(13) Getman, E.; Loboda, S.; Ignatov, A.; Demchenko, P. *Pol. J. Chem.* **2004**, *78*, 35−43.
(14) Kurova, T. A.; Shumyatskaya, N. G.; Voronkov, A. A.; Pyatenko, Yu.A. *Dokl. Akad. Nauk SSSR* **1980**, *251*, 605−607.
(15) Chen, H.; Hautier, G.; Ceder, G. *J. Am. Chem. Soc.* **2012**, *134*, 19619−19627.
(16) Vasiliev, A.; Volkova, O.; Baranov, A.; Presniakov, I.; Sobolev, A.; Demazeau, G.; Stone, M.; Zheludev, A.; Klingeler, R.; Büchner, B. *J. Phys.: Condensed Matter* **2010**, *22*, 016007.
(17) Zheludev, A.; Maslov, S.; Shirane, G.; Sasago, Y.; Koide, N.; Uchinokura, K. *Phys. Rev. Lett.* **1997**, *78*, 4857.
(18) Goodenough, J. B. *Magnetism and the Chemical Bond*; Robert E. Krieger Publishing Co.: Huntington, NY, 1976.
(19) Yu, J.-T.; Huang, Y.-S.; Lin, S.-S. *J. Phys.: Condens Matter* **1990**, *2*, 5587−5594.
(20) Basu, P.; Chakravorty, A. *Inorg. Chem.* **1992**, *31*, 4980−4986.
(21) Brown, D.; Altermatt, D. *Acta Crystallogr.* **1985**, *B41*, 244−247.